Available online at www.sciencedirect.com
ScienceDirect
Trans. Nonferrous Met. Soc. China 33(2023) 2155−2167
Transactions of Nonferrous Metals Society of China
www.tnmsc.cn

Synthesis of h-MoO_3 nanorods and h-/α-MoO_3 composites and their photocatalytic performance

Lu WANG[1], Hong-xiao LI[2], Zheng-liang XUE[1,2]

1. State Key Laboratory of Refractories and Metallurgy, Wuhan University of Science and Technology, Wuhan 430081, China;
2. Key Laboratory for Ferrous Metallurgy and Resources Utilization of Ministry of Education, Wuhan University of Science and Technology, Wuhan 430081, China

Received 13 February 2022; accepted 4 July 2022

Abstract: A facile hydrothermal route for the synthesis of h-MoO_3 nanorods and h-/α-MoO_3 composites was proposed. XRD, TG−DSC, FESEM−EDX, TEM, FT-IR, Raman, photoluminescence (PL) and UV−vis DRS spectroscopy were used to characterize the as-synthesized products. h-MoO_3 was formed when the liquid/solid ratio of the raw materials was 2:1 and 5:1. However, homogeneous h-/α-MoO_3 composites were obtained when the liquid/solid ratio was increased to 8:1 and 12:1. A possible mechanism by which h-MoO_3 is formed, and its transformation into α-MoO_3 were investigated. h-MoO_3 annealing was found to comprise three mass-loss stages; i.e., the removal of each of the following: physically adsorbed water, residual ammonium, and coordinated water. Both h-MoO_3 nanorods and h-/α-MoO_3 composites demonstrated excellent visible-light-driven photocatalytic performance with regard to methylene blue degradation. The superior degradation efficiency of the h-/α-MoO_3 composites was ascribed to a lower recombination rate of electron−hole pairs, a reduced band gap energy, and an enhanced synergistic effect.
Key words: h-MoO_3; α-MoO_3; hydrothermal synthesis; photocatalytic performance; methylene blue

1 Introduction

Hexagonal molybdenum trioxide (h-MoO_3, space group: $P6_3/m$), which is a metastable phase of MoO_3 polymorphs, has a unique one-dimensional structure. A tunnel with a diameter of 3.0−3.5 Å runs along the c direction. It is enclosed by twelve [MoO_6] octahedrons linked by sharing corners along the a and b directions, as well as edges along the c direction [1]. The tunnel may contain mobile monovalent cations and water molecules, and is highly suitable for insertion reactions [2].

Owing to the large tunnel and the spatially open layered structure, h-MoO_3 exhibits numerous potentially useful physicochemical properties, such as photoluminescence, photochromism, electrochromism, photocatalytic activity, and gas sensor properties, when compared with the thermodynamically stable orthorhombic phase (α-MoO_3, space group: $Pnma$) [3−5]. It has recently been reported that h-/α-MoO_3 composites have better photochromic properties than single-phase h-MoO_3 nanorods (NRs) when irradiated with sunlight [6]. Consequently, both h-MoO_3 nanorods (NRs) and h-/α-MoO_3 composites are now amongst the most promising candidates for use in applications such as smart windows, chemical sensors, photocatalysts, and lithium ion batteries [7−9]. Therefore, the controllable synthesis of h-MoO_3 NRs and h-/α-MoO_3 composites has received increasing attention in recent years.

In the past decades, we have witnessed rapid advances in the synthesis of various MoO_3 nano-

Corresponding author: Lu WANG, Tel: +86-15600563937, E-mail: wanglu@wust.edu.cn
DOI: 10.1016/S1003-6326(23)66250-8

materials [10]. α-MoO_3, which has diverse morphologies, has been widely investigated [11−15]. However, h-MoO_3 and h-/α-MoO_3 composites have received relatively little attention. The most common strategy for their synthesis is the hydrothermal method, which uses various Mo sources (e.g., $MoO_2(OH)(OOH)$, $Na_2MoO_3{\cdot}2H_2O$, $(NH_4)_6Mo_7O_{24}{\cdot}4H_2O$ (AHM), and $(NH_4)_2Mo_4O_{13}{\cdot}H_2O$) and acids (e.g., HNO_3, HCl, and H_2SO_4) as raw materials [16,17]. In the present work, a modified hydrothermal route for the synthesis of h-MoO_3 and h-/α-MoO_3 composites is proposed, in which solid AHM is directly mixed with liquid HNO_3 in an autoclave without the necessity of forming an AHM solution in deionized water. When compared with the syntheses reported in the literature [18−20], the current method is simple because it omits the formation of an ionic liquid and the step of ultrasonic treatment. However, ZHENG et al [21] used pure Mo powder, which is expensive, as the Mo source material; this increased the economic costs. Moreover, the synthesis was also complex. The method proposed in the present work is relatively simple. The influence of various liquid/solid ratios of the raw materials (defined as the ratio of the volume of liquid HNO_3 to the mass of solid AHM) on the characteristics of the as-synthesized products, the nucleation–growth mechanism of h-MoO_3, and the mechanism by which h-MoO_3 is transformed into α-MoO_3, were investigated. The photocatalytic performance of the as-synthesized h-MoO_3 and h-/α-MoO_3 composites with regard to the degradation of methylene blue (MB) was also investigated.

2 Experimental

2.1 Synthesis

Concentrated nitric acid and reagent-grade ammonium heptamolybdate tetrahydrate (AHM; $(NH_4)_6Mo_7O_{24}{\cdot}4H_2O$) were selected as the raw materials, and were used without further purification. In a typical experimental process, 20 mL of liquid HNO_3 and 10 g of solid AHM were added directly to a 100 mL parapolyphenol-lined stainless steel autoclave. The autoclave containing the raw materials was then heated in an oven at 423 K for 12 h. After cooling to room temperature (RT), the white precipitate was collected and filtered several times with deionized water and ethanol, and the final product was dried at 323 K for 5 h. Various liquid/solid ratios of raw materials (2:1, 5:1, 8:1, and 12:1) were used to determine the influence of the ratio on the characteristics of the as-synthesized samples. The samples synthesized using liquid/solid ratios of 2:1, 5:1, 8:1, and 12:1 were named Samples S1, S2, S3, and S4, respectively.

2.2 Characterization

The crystallographic structures of the as-synthesized samples were characterized using various technologies, e.g., X-ray diffraction (XRD; TTR III; Rigaku Corporation, Japan), field-emission scanning electron microscopy (FESEM; ZEISS SUPRA 55; ZEISS, Oberkochen, Germany), high-resolution Raman spectroscopy (HR-RS; LabRAM HR Evolution; HORIBA Jobin YvonS. A. S., France), Fourier-transform infrared spectroscopy (FT-IR; INVENIO R, BRUKER Germany), transmission electron microscopy (TEM), and selected area electronic diffraction analysis (SAED; Tecnai^{TM} G2 F30 S-TWIN; FEI Corporation, USA). Photoluminescence (PL) spectroscopy (using an F−7100 FL spectrophotometer with an excitation wavelength of 325 nm) and UV−vis diffuse reflectance spectroscopy (DRS; UV−5500PC) were also adopted to determine the optical properties of the samples.

2.3 Photocatalytic performance

MB dye was used as a typical model material to examine the photocatalytic performance of the as-synthesized samples. First, 100 mg of catalyst was added to a beaker containing 200 mL of MB solution (20 mg/L). The solution was stirred in a magnetic stirrer at 600 r/min in the dark for various time to establish an adsorption–desorption equilibrium on the surface of the catalyst. Subsequently, the residual liquid was irradiated with visible light from a 300 W Xe lamp source. The distance between the light source and the solution surface was 10 cm. After illumination for a period of time, the solution was collected by centrifugation. The absorbance behavior of the MB solution before and after irradiation was monitored using a UV−vis spectrophotometer in the wavelength range of 200−800 nm.

3 Results and discussion

3.1 XRD analysis

Figure 1 shows the XRD patterns of the as-synthesized samples obtained at various liquid/solid ratios of raw materials. When the liquid/solid ratio was 2:1, Sample S1 was clearly identified as *h*-MoO_3 (PDF card No. 21-569). No peaks attributable to other species were detected, indicating the high purity of the as-synthesized *h*-MoO_3. When the liquid/solid ratio was increased to 5:1, *h*-MoO_3 was the only detectable product. However, when the liquid/solid ratio was increased to 8:1, peaks attributable to both *h*-MoO_3 and *α*-MoO_3 (PDF card No. 65-2421) were detected, suggesting their co-existence in Sample S3. When the liquid/solid ratio was further increased to 12:1, another diffraction peak was detected, which was attributed to $MoO_3(H_2O)_2$ (PDF card No. 70-1513). The XRD patterns suggest that the phase composition was closely related to the liquid/solid ratios of the raw materials; in other words, the phase transformation from *h*-MoO_3 to *α*-MoO_3 happened as the amount of HNO_3 was increased.

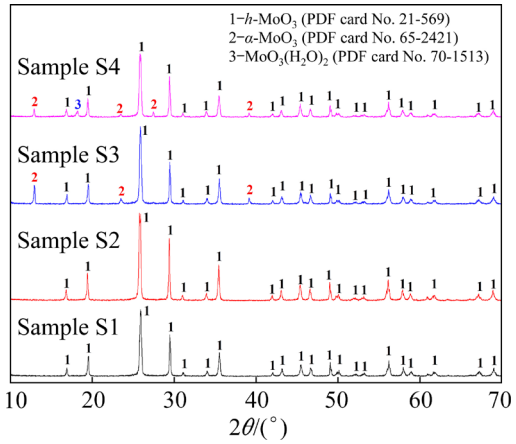

Fig. 1 XRD patterns of as-synthesized products obtained at various liquid/solid ratios of raw materials

3.2 Thermal analysis

To investigate the thermal properties of the as-synthesized samples, thermogravimetry–differential scanning calorimetry (TG−DSC) curves were obtained, as shown in Fig. 2. Sample S1 was selected as the analytical product, and the curves were obtained under an Ar atmosphere from RT to 824 K at a heating rate of 10 K/min, followed by cooling to RT again at a rate of 10 K/min in the same Ar atmosphere.

In Fig. 2, the mass loss (w_t) of the sample was calculated using the following equation:

$$w_t = \frac{m_t - m_0}{m_0} \times 100\% \quad (1)$$

where m_0 and m_t are the mass of the sample at the beginning and the mass of the sample after reaction for a period of time t, respectively. The TG curves reveal that the total mass loss of the sample can be divided into three stages, which can be defined as Δm_1, Δm_2, and Δm_3. Herein, the values of Δm_1, Δm_2,

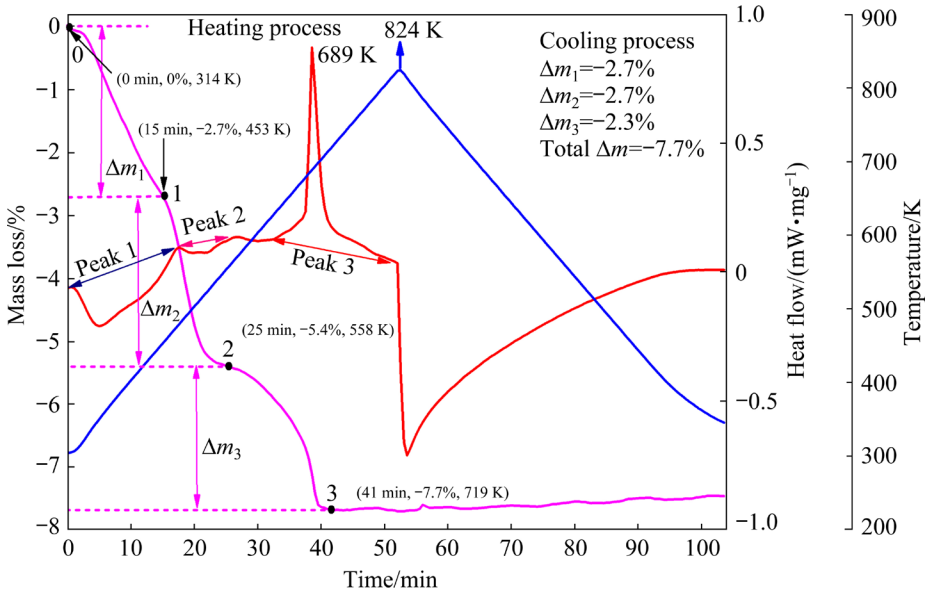

Fig. 2 TG−DSC curves of as-synthesized *h*-MoO_3 (Sample S1) recorded from RT to 824 K under Ar atmosphere at heating rate of 10 K/min followed by cooling to RT again at rate of 10 K/min in same Ar atmosphere

and Δm_3 were calculated using Eqs. (2), (3), and (4), respectively.

$$\Delta m_1 = w_{t_1} - w_{t_0} \quad (2)$$

$$\Delta m_2 = w_{t_2} - w_{t_1} \quad (3)$$

$$\Delta m_3 = w_{t_3} - w_{t_2} \quad (4)$$

where w_{t_n} is the mass loss of the sample after reaction for a period of time t_n. When the temperature increased to 314 K, the mass of the sample began to decrease; the time was considered to be the initial time, t_0=0 min. Subsequently, the mass loss increased as the temperature increased. When the temperature reached 453 K (reaction time t_1=15 min), an obvious inflection point was observed with a mass loss of approximately Δm_1=−2.7%, which was due to the evaporation of physically adsorbed water. Peak 1 on the DSC curve indicates that the first mass loss stage was an endothermic process. As the temperature further increased to 558 K (reaction time t_2=25 min), a second inflection point occurred (see Point 2); at this point, the total mass loss w_{t_2} equaled −5.4%. It was possible to deduce the second mass loss stage Δm_2=−2.7% using Eq. (3). The mass loss of Δm_2 may be ascribed to the liberation of volatile by-products associated with ammonium decomposition in the sample, and it resulted in the small endothermic (Peak 2). When the temperature increased to 719 K (reaction time t_3=41 min), there was a third mass loss process (see Point 3). In that case, the total mass loss w_{t_3} was −7.7% and a third mass loss stage Δm_3=−2.3% was deduced. The mass loss of Δm_3 may be attributed to the release of coordinated water in the tunnel from the internal structure of *h*-MoO_3 [22]. There was also a strong exothermic peak at 689 K on the DSC curve (Peak 3), which may be attributed to the irreversible phase transformation from *h*-MoO_3 to *α*-MoO_3. The transformation temperature agreed well with the temperatures reported in other publications [23,24]. Figure 2 reveals no mass or thermal changes on the TG−DSC curves during the cooling process. This indicates that *α*-MoO_3 did not transform back to *h*-MoO_3 in the low-temperature stage, further suggesting the metastable property of the as-synthesized *h*-MoO_3.

3.3 FT-IR and Raman spectra analyses

Fourier-transform infrared (FT-IR) absorption spectroscopy was also used to characterize *h*-MoO_3 (Sample S1), and the results are shown in Fig. 3(a). The absorption peaks at 3520.47 and 1613.61 cm^{-1} were ascribed to the stretching mode of O—H group and the bending mode of H—O—H in H_2O, respectively, indicating the presence of physically adsorbed water. The absorption peaks at 3225.28 and 1415.08 cm^{-1} were attributed to the N—H stretching and bending vibrations of the $[NH_4]^+$ groups, respectively, which revealed the presence of residual $[NH_4]^+$. The FT-IR spectrum results further confirmed the presence of residual physically-adsorbed water and ammonium, which agreed well with the TG−DSC curves shown in Fig. 2 and provided in the literature [22,25]. The vibrational peak at 970.98 cm^{-1} was ascribed to the characteristic stretching mode of Mo═O double bond of *h*-MoO_3, and the peak at 798.01 cm^{-1} corresponded to Mo—O—Mo vibrations. Raman spectroscopy was also used to characterize the as-synthesized *h*-MoO_3 (Sample S1). The peaks at 980.85, 905.96, and 888.7 cm^{-1} shown in Fig. 3(b) were attributed to the Mo═O double bond, and the peaks at 693.92, 499.13, 419.60, 403.08, and

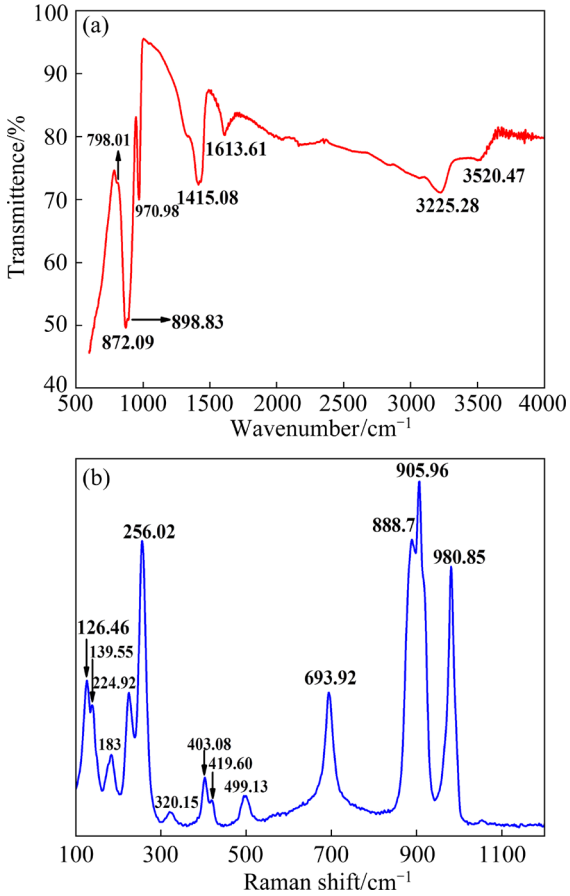

Fig. 3 FT-IR (a) and Raman (b) spectra of as-synthesized *h*-MoO_3 in Sample S1

320.15 cm^{-1} were assigned to the O—Mo—O vibrations. The peaks between 256.02 and 126.46 cm^{-1} represent the skeletal modes of the chains of MoO_4 tetrahedra [26].

According to the analysis described above, the actual chemical formula of the as-synthesized *h*-MoO_3 (Sample S1) can be modified to $MoO_{3-a}(NH_4)_b(H—OH)_c$, where *a* represents oxygen vacancies, and *b* and *c* represent the numbers of residual ammonium and water molecules, respectively. The reason for their absences in the XRD pattern may have been due to the small amounts of *b* and *c*. Therefore, the formation of $MoO_{3-a}(NH_4)_b(H—OH)_c$ may be expressed by Eq. (5):

$$(NH_4)_6Mo_7O_{24}\cdot 4H_2O(aq)+HNO_3(aq) \xrightarrow[\text{autoclave}]{423\ K,\ 12\ h} MoO_{3-a}(NH_4)_b(H—OH)_c(aq)+NH_4NO_3(aq)+H_2O(l) \quad (5)$$

The mass loss processes of the three stages shown in Fig. 2 during the heating process can be expressed using Eqs. (6)−(8), respectively:

$$MoO_{3-a}(NH_4)_b(H—OH)_c \xrightarrow[Ar]{314-453\ K} MoO_{3-a}(NH_4)_b(H—OH)_d(s)+(c-d)H_2O(g) \quad (6)$$

$$MoO_{3-a}(NH_4)_b(H—OH)_d(s) \xrightarrow[Ar]{453-558\ K} MoO_{3-a}(H—OH)_d(s)+bNH_3(g) \quad (7)$$

$$MoO_{3-a}(H—OH)_d(s) \xrightarrow[Ar]{558-719\ K} \alpha\text{-}MoO_3+dH_2O \quad (8)$$

3.4 Microstructure examination

3.4.1 FESEM analysis

Figure 4 shows the morphology evolution of the as-synthesized products formed from various liquid/solid ratios of raw materials. When Sample S1 was examined, the as-synthesized *h*-MoO_3 was found to comprise perfect hexagonal rod-like structures with clear faces and edges. They were 50−200 nm in diameter and several micrometers long (Figs. 4(a_1−a_3)). The *h*-MoO_3 NRs grew outward rather than inward, and their gross images appeared to show distinct flower-like structures. When the liquid/solid ratio of the raw materials was increased to 5:1 (Sample S2), the hexagonal structures of *h*-MoO_3 NRs began to collapse and their surface cross-sections became rough (Figs. 4(b_1−b_3)). When the liquid/solid ratio was further increased to 8:1 (Sample S3), the surface structure of the product became much rougher and each particle consisted of several small platelet- or

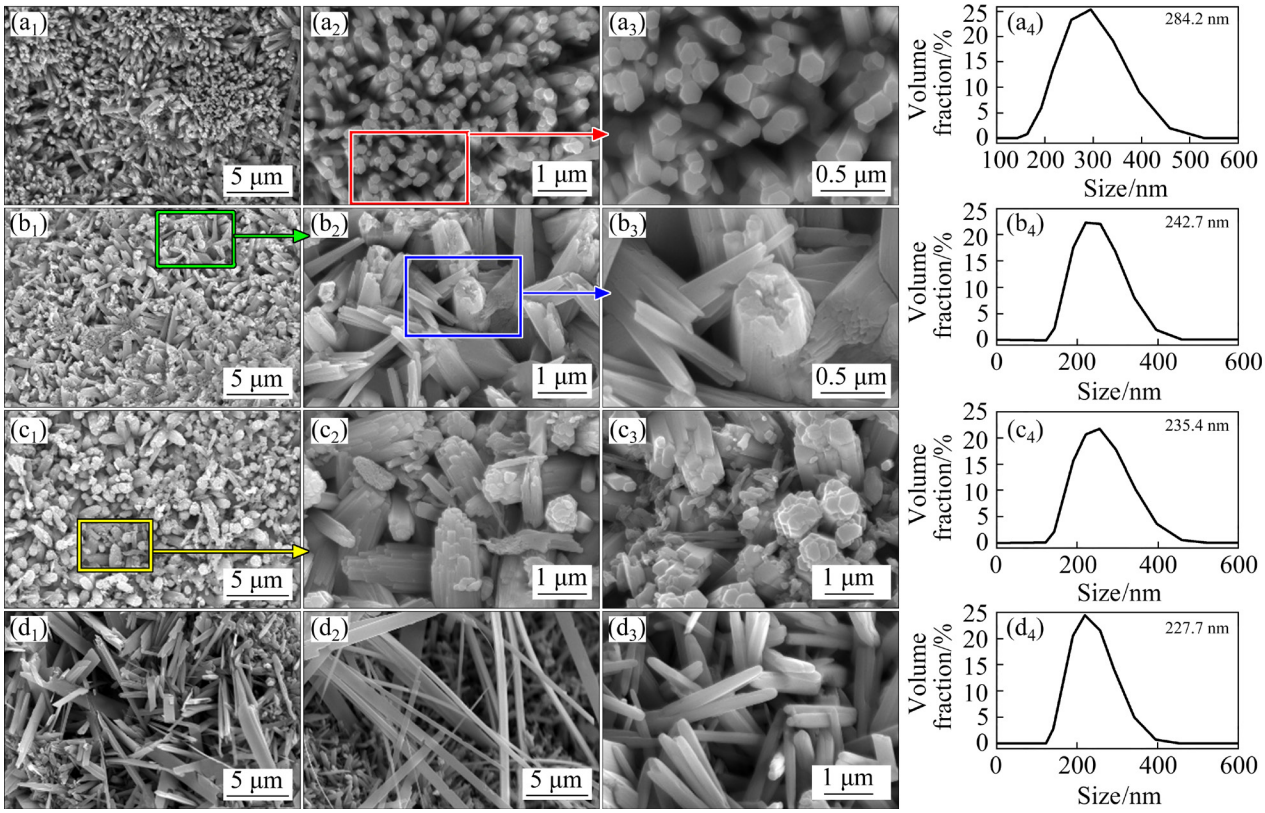

Fig. 4 FESEM micrographs and particle size distribution diagrams of as-synthesized products produced using various liquid/solid ratios of raw materials: (a_1−a_4) Sample S1; (b_1−b_4) Sample S2; (c_1−c_4) Sample S3; (d_1−d_4) Sample S4

rod-shaped crystals (Figs. 4(c_1−c_3)). Combined with the XRD results described above, these results suggested that the product of Sample S3 could be described as *h*-/*α*-MoO_3 composites. The number of platelet-shaped *α*-MoO_3 structures that were several nanometers thick increased rapidly when the liquid/solid ratio increased to 12:1 (Sample S4), as shown in Figs. 4(d_1−d_3); i.e., the number of *α*-MoO_3 nanoplatelets (NPs) increased as the H^+ concentration increased. The FESEM results also indicated that the morphology of the as-synthesized products changed from one-dimensional hexagonal nanorods to two-dimensional layered structures as the liquid/solid ratio of the raw materials increased. The average sizes of the products in the four samples (S1, S2, S3, and S4) were 284.2, 242.7, 235.4, and 227.7 nm, respectively (Figs. 4(a_4−d_4)), which also indicated that the increase in H^+ concentration reduced the particle sizes of the as-synthesized products.

3.4.2 Elemental composition

Figure 5 shows the EDX spectra of the as-synthesized products produced using various liquid/solid ratios of raw materials. The peaks at 0.525 and 2.4 keV confirmed the presence of O and Mo atoms in the as-synthesized products. The appearance of the peak attributable to C at 0.2 keV was due to the conducting resin. Although there was a peak attributable to N at 0.4 keV, its intensity was very low and its concentration can be ignored. The mass fraction and molar fraction of O and Mo are tabulated as an inset in Fig. 5. Quantification of the peaks gave the O/Mo atomic ratios of 4.11, 3.50, 2.83, and 2.28 for Samples S1, S2, S3, and S4, respectively. Deviations of their O/Mo atomic ratios from 3 may have been due to the presence of adsorbed water, oxygen vacancies, or measuring errors.

3.4.3 TEM analysis

The TEM results displayed in Figs. 6(a_1−a_3) revealed the hexagonal shape and well-defined single-crystalline structure of the as-synthesized *h*-MoO_3 in Sample S1. The lattice spacing of the *h*-MoO_3 (Sample S1) was calculated as 0.9161 nm, which agreed well with the value for a (100) crystal plane. The growth of *h*-MoO_3 NRs along the (100)

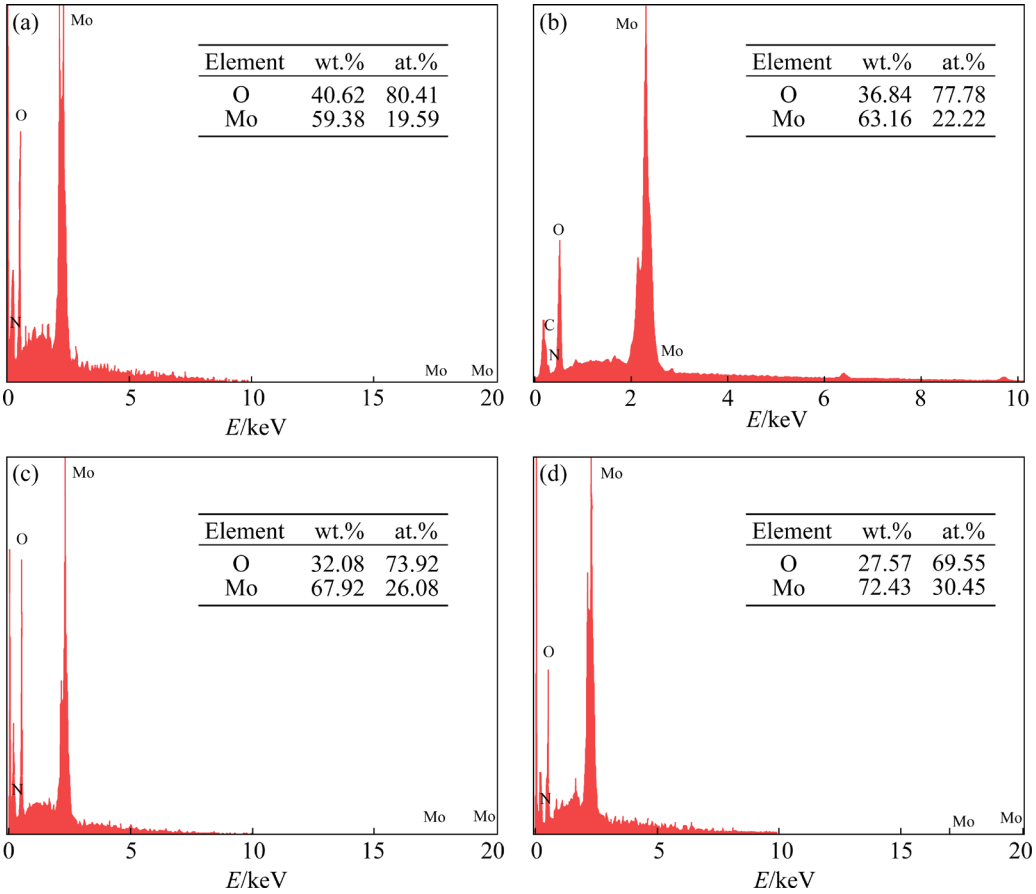

Fig. 5 EDX spectra of as-synthesized products produced using various liquid/solid ratios of raw materials: (a) Sample S1; (b) Sample S2; (c) Sample S3; (d) Sample S4

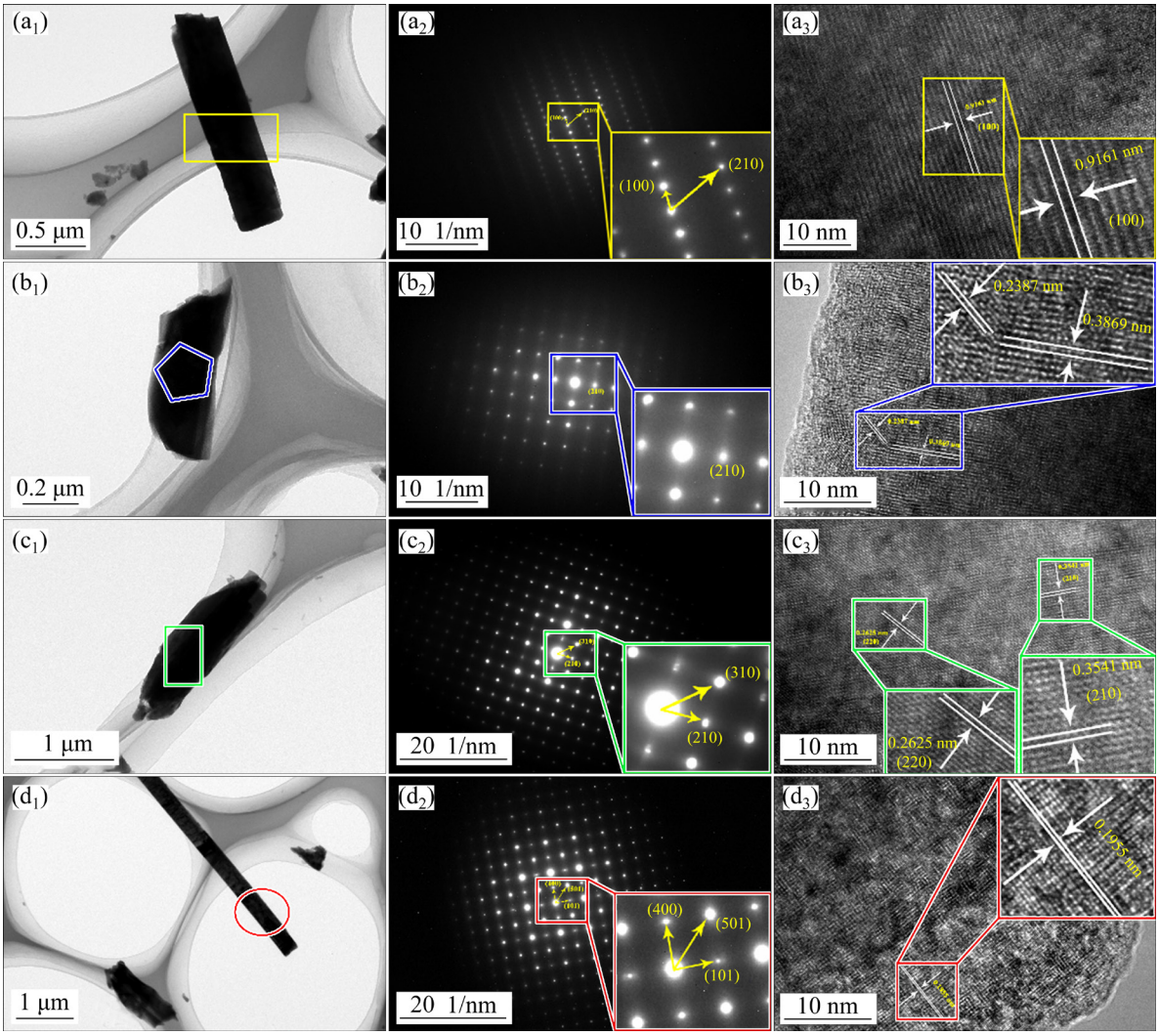

Fig. 6 TEM micrographs of as-synthesized products produced using various liquid/solid ratios of raw materials: (a_1−a_3) Sample S1; (b_1−b_3) Sample S2; (c_1−c_3) Sample S3; (d_1−d_3) Sample S4

direction could also be inferred from the results shown in Figs. 6(a_1−a_3). When the liquid/solid ratios of raw materials increased to 5:1 (Sample S2) and 8:1 (Sample S3), the as-synthesized products had rougher surface structures; some lattice dislocations appeared even though their single-crystalline structures remained. Both platelet- and rod-shaped structures were present when the liquid/solid ratio of the raw materials was increased to 12:1 (Sample 4), as shown in Fig. 6(d_1). Over all, the TEM results agreed well with those obtained by FESEM.

3.5 Formation mechanism of *h*-MoO_3 and *α*-MoO_3

As is known, the [MoO_6] octahedron is the basic building block of both *h*-MoO_3 and *α*-MoO_3. Only one Mo—O—Mo connection is formed if two octahedrons are linked by a corner; however, two Mo—O—Mo connections are formed if they are linked by an edge. Compared with a linked corner, two octahedrons linked by an edge have a lower energy [27]. That is why *α*-MoO_3 is the thermodynamically stable phase and *h*-MoO_3 is the metastable phase. However, *h*-MoO_3 rather than *α*-MoO_3 was formed first in the present study, which was hard to understand. This phenomenon may be explained as follows. Initially, strong interactions between AHM and HNO_3 take place at 423 K in a high-pressure environment. Subsequently, the [MoO_6] octahedron is formed via a spontaneous reaction between the Mo and O atoms. The newly-formed octahedron then interlinks through the cis-position with the

assistance of NH_4^+ and OH^- groups. It has been suggested that the NH_4^+ and OH^- groups in the internal structure of MoO_3 act as structure-directing and stabilizing agents in the *h*-MoO_3 nanocrystals rods [22]. In other words, NH_4^+ groups may contribute to edge sharing along the *c*-axis, and OH^- groups may be beneficial to corner sharing along the *a*-axis. This could lead to the anisotropic growth of *h*-MoO_3 in a preferred orientation. According to classical nucleation–growth theory, numerous MoO_3 crystal nuclei are formed through a diffusion mechanism when the actual solubility is greater than its equilibrium value; subsequently, the growth process proceeds. That is to say, the energy required for the activation of MoO_3 crystal nucleation from the mother liquor is greater than that required for their growth. The interface energy between the crystal nucleus and the mother liquor also exerts an important influence on the formation of the new phase, as described by Eq. (9) [28]. If the structure of a new nucleus is similar to that of the mother liquor, the energy barrier for nucleation is greatly reduced, and the new phase is preferentially precipitated. Because *h*-MoO_3 and the mother liquor had similar network structures, *h*-MoO_3 rather than *α*-MoO_3 was formed first. Similar explanations have been given in other publications [29−31].

$$\Delta G_{\text{hom}}^{*} = 1/3A^{*} \cdot \sigma \tag{9}$$

where $\Delta G_{\text{hom}}^{*}$ is the critical Gibbs free energy change for the homogeneous nucleation; A^* is the surface area of the critical nucleus; σ is the interface energy between the new nucleus and the mother liquor. Once the *h*-MoO_3 cores were formed, the subsequent process proceeded readily through heterogeneous nucleation owing to much lower Gibbs free energy change, as described by [28]

$$\frac{\Delta G_{\text{het}}^{*}}{\Delta G_{\text{hom}}^{*}} = \frac{2 - 3\cos\theta + \cos^3\theta}{4} \tag{10}$$

where $\Delta G_{\text{het}}^{*}$ is the critical Gibbs free energy change for the heterogeneous nucleation; θ is the contact angle. Furthermore, high-pressure hydrothermal reactions usually generate a special subcritical or supercritical state. Therefore, the reaction between AHM and HNO_3 probably proceeded at a molecular level, which would have greatly enhanced the activities of reactive species; consequently, new chemical reactions occurred and *h*-MoO_3 was formed first in a short time [29]. Increasing the liquid/solid ratio of the raw materials to 8:1 or 12:1 (Samples S3 and S4) increased the H^+ concentration in the mother liquor. The excess H^+ then reacted with the NH_4^+ and OH^- groups, which reduced their concentrations. Consequently, the structural stabilization of *h*-MoO_3 was impeded, and the as-formed *h*-MoO_3 collapsed and exfoliated into numerous platelet-shaped particles. In other words, the *h*-MoO_3 NRs were dissolved and recrystallized into *α*-MoO_3 NPs; i.e., a dissolution–recrystallization mechanism existed during the hydrothermal process as the H^+ concentration increased. A possible mechanism by which the *h*-MoO_3 NRs and *α*-MoO_3 NPs were produced using the various liquid/solid ratios of raw materials is presented schematically in Fig. 7.

3.6 Analysis of optical property and photocatalytic performance

3.6.1 Optical property

MoO_3 can absorb photons with energies that exceed its forbidden energy gap, and generate excited electrons that transform from the basic state to the excitation state, and then photo-generated electron-hole pairs are formed. However, the electrons in the excitation state may return to the basic state and recombine with the holes to produce fluorescence [20]. PL spectroscopy was adopted to estimate the recombination rate of the photo-generated electrons and holes, which is an important optical property of *h*-MoO_3. Because the phase compositions of Samples S1/S2 and S3/S4 comprised single-phase *h*-MoO_3 NRs and *h*-/*α*-MoO_3 composites, respectively, only Samples S1 and S3 were selected for the subsequent analyses. Figure 8 shows the PL spectra of Samples S1 and S3. The spectra revealed that the PL intensity of Sample S3 was lower than that of Sample S1, indicating a lower recombination rate of photo-generated electrons and holes in Sample S3. The lower PL intensity of Sample S3 may indicate its higher photocatalytic activity.

3.6.2 Photocatalytic performance

Figure 9 shows the absorption–photocatalysis performances of Samples S1 and S3. Figure 9(a) revealed that the absorption efficiency of Sample S1 increased gradually over time in the initial stage; after 0 min (adsorption time: 60 min), the

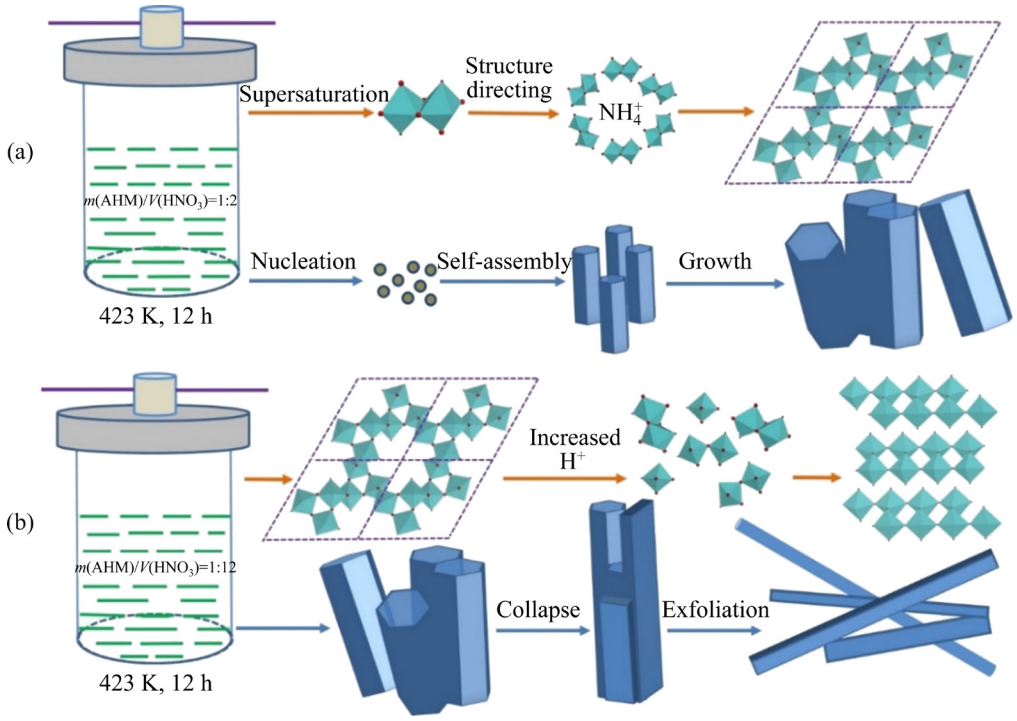

Fig. 7 Proposed possible formation mechanisms of h-MoO_3 NRs (a) and α-MoO_3 NPs (b)

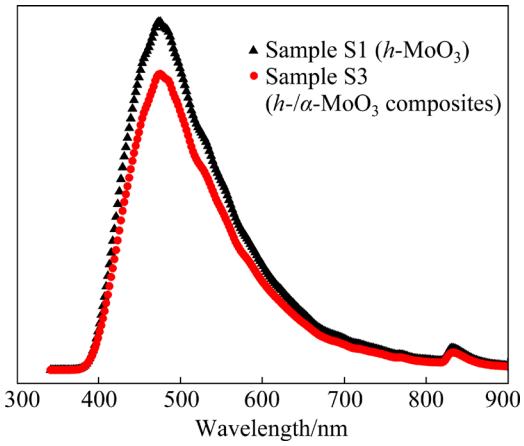

Fig. 8 PL spectra of Samples S1 (single-phase h-MoO_3) and S3 (h-/α-MoO_3 composites)

absorption efficiency was hardly changed, indicating the establishment of an absorption–desorption equilibrium between the MB solution and h-MoO_3 catalyst. The absorbance of MB solution decreased rapidly after turning on the light, and it changed from blue to colorless over 120 min. The behavior of Sample S3 was similar to that of Sample S1.

To make an intuitive comparison of the absorption–photocatalysis performances of Samples S1 and S3, their degradation efficiency (α) values were calculated using the following formula:

$$\alpha = -\frac{A_t - A_0}{A_0} \times 100\% \quad (11)$$

where A_0 and A_t are the absorbances of the sample at the initial time (−60 min) and the absorbance after reaction for a period of time t, respectively. Figure 9(b) shows the calculated results for the degradation efficiency of Samples S1 and S3 after various reaction time, from which it could be seen that the MB degradation efficiency of Sample S3 was always greater than that of Sample S1, except for in the final stage, indicating the larger absorption–photocatalysis performance of Sample S3. SONG et al [6] investigated the photochromic properties of h-MoO_3 microrods and h-/α-MoO_3 composites, and concluded that h-/α-MoO_3 composites have better photochromic properties than h-MoO_3 microrods when irradiated by sunlight. The current results agreed well with those reported by SONG et al [6].

The degradation efficiencies of various MoO_3 species with regard to MB dye under various conditions are summarized in Table 1. Generally, the efficiency of visible light assisted MB degradation could be effectively improved by increasing the catalyst concentration and degradation time. However, the efficiency declined

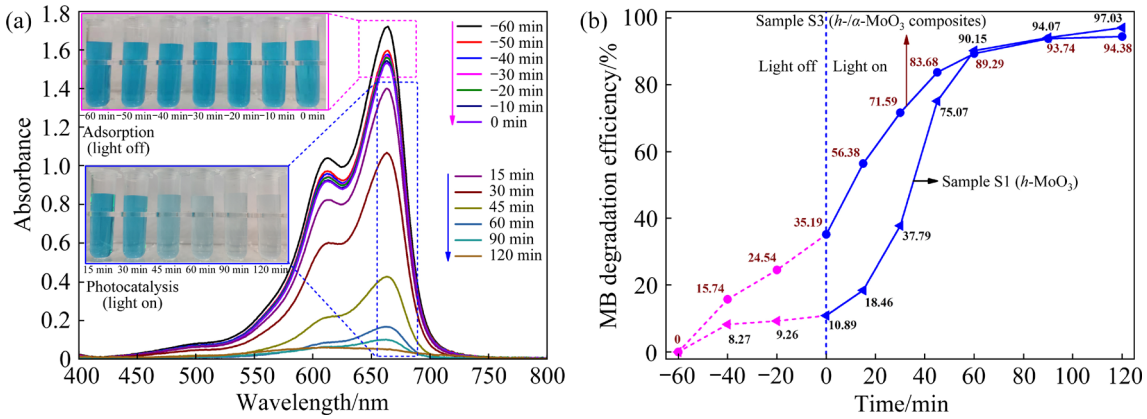

Fig. 9 Absorption–photocatalysis performances of as-synthesized samples: (a) Spectral evaluation of MB degradation by Sample S1; (b) MB degradation efficiency vs reaction time (The negative and positive reaction times represent the absorption and photocatalysis processes, respectively)

Table 1 Comparison of MB degradation efficiencies of various MoO_3 species under visible light

Material	MB concentration/ ($mg·L^{-1}$)	Catalyst concentration/ ($mg·L^{-1}$)	Time/ min	Degradation efficiency/%	Source
α-MoO_3	10	1000	210	81.2	[32]
ZIF-8	10	500	120	82.3	[33]
h-MoO_3 nanocrystals	10	1000	120	90.74	[34]
h-MoO_3 nanocrystals	12	200	120	86.61	[22]
h-MoO_3 microrods	10	500	180	97	[35]
3 at.% Dy-doped MoO_3	10	500	50	97.76	[36]
Ce(5)/MoO_3	5	500	50	89	[37]
h-MoO_3 nanorods	20	500	120	97.03	This work
h-/α-MoO_3 composites	20	500	120	94.38	This work

as the initial dye concentration increased. Even though the MB concentration used in the present work was up 20 mg/L, the degradation efficiency with regard to MB dye was still very high when compared with the results reported in the literature. Therefore, it can be inferred that the as-synthesized h-MoO_3 and h-/α-MoO_3 composites investigated in the present study exhibited better photocatalysis performances.

Figure 10 shows the UV−vis diffuse reflectance spectra of Samples S1 and S3. The reflectance edges of Samples S1 and S3 were 485 and 480 nm, respectively, which indicated that both samples had strong visible light absorption capacities. In general, band gap energy (E_g) is considered a critical parameter for determining the photoreaction activity of a material, so the superior absorption–photocatalysis performances of Samples S1 and S3 can also be explained by their band gap energies [6]. Herein, the Kubelka–Munk (K−M) re-emission function $F(R)$ was used to predict the band gap energies of Samples S1 and S3 based on the following equation [38]:

$$F(R)=\frac{(1-R)^2}{2R} \tag{12}$$

where R is the diffuse reflectance of an infinitely thick sample. $F(R)$ is the re-emission or K−M functions, which is related to the absorption constant of the material:

$$F(R)\propto\alpha=\frac{(h\nu-E_g)^n}{h\nu} \tag{13}$$

where α is the absorption constant; h is Planck's constant; ν is the photo frequency; $h\nu$ is the incident photo energy; E_g is the band gap energy; n is a parameter connected to the distribution of the optical transition process in the band gap region.

The value of n is either equal to 0.5 for direct transition or equal to 2 for indirect transition [25]. With regard to MoO_3, n is equal to 2 [6,21]. By extrapolating the intercept of the plots of $(Fhv)^{0.5}$ against (hv), it is possible to determine E_g, as shown in the inset of Fig. 10. From the intercept of the horizontal axis it can be seen that the calculated band gap energies of Samples S1 and S3 were 2.81 and 2.75 eV, respectively. The lower band gap energy of Sample S3 was responsible for its higher visible-light-driven photocatalysis performance.

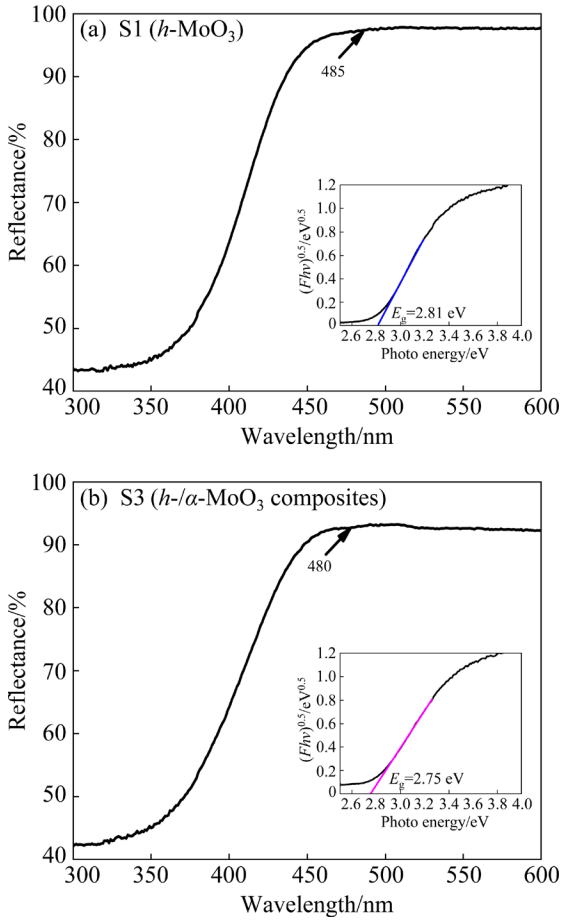

Fig. 10 UV−vis diffuse reflectance spectra of Sample S1 (a) and Sample S3 (b)

When comparing the particle sizes of Samples S1 (284.2 nm) and S3 (235.4 nm) shown in Fig. 4, it can be inferred that Sample S3 may have a larger specific surface area than Sample S1. Therefore, Sample S3 exhibited a stronger adsorption property (Fig. 9), which further facilitated its photocatalytic performance. That is to say, the synergistic relationship between adsorption and photocatalysis may also have played an important role in improving the MB degradation efficiency of Sample S3 [39].

4 Conclusions

(1) It was possible to divide the annealing process of h-MoO_3 NRs into three mass loss stages during heating from RT to 824 K. The three stages were due to the evaporation of physically adsorbed water, the decomposition of ammonium, and the liberation of the coordinated water in the tunnel.

(2) $[NH_4]^+$ in solution directed and stabilized the formation of h-MoO_3 NRs when the liquid/solid ratios of the raw materials were 2:1 and 5:1. When the liquid/solid ratios of the raw materials was increased to 8:1 and 12:1, the effect of $[NH_4]^+$ diminished and the h-/α-MoO_3 composites were formed.

(3) Because of the lower recombination rate of photo generated electron−hole pairs, the reduced band gap energy, and the higher synergistic effect between adsorption and photocatalysis, the h-/α-MoO_3 composites exhibited higher visible-light-driven photocatalysis performance with regard to MB degradation.

Acknowledgments

The authors are grateful for the financial supports from the National Natural Science Foundation of China (No. 52104310). We also would like to thank the Analytical & Testing Center of Wuhan University of Science and Technology (China) for the help.

References

[1] PAN Wen-zhi, TIAN Rui-yuan, JIN Hao, GUO Yan-jun, ZHANG Li-ping, WU Xiao-chun, ZHANG Li-na, HAN Zhi-hua, LIU Guang-yao, LI Jian-bo, RAO Guang-hui, WANG Han-fu, CHU Wei-guo. Structure, optical, and catalytic properties of novel hexagonal metastable h-MoO_3 nano- and microrods synthesized with modified liquid-phase processes [J]. Chemistry of Materials, 2010, 22: 6202−6208.

[2] CABELLO M, MEDINA A, ALCANTARA R, NACIMIENTO F, PEREZ-VICENTE C, TIRADO J. A theoretical and experimental study of hexagonal molybdenum trioxide as dual-ion electrode for rechargeable magnesium battery [J]. Journal of Alloys and Compounds, 2020, 831: 154795.

[3] KUMAR S, SINGH A, SINGH R, SINGH S, KUMAR P, KUMAR R. Facile h-MoO_3 synthesis for NH_3 gas sensing application at moderate operating temperature [J]. Sensors and Actuators B: Chemical, 2020, 325: 128974.

[4] GHALEHGHAFI E, RAHMANI M. B. Hydrothermal temperature effect on the growth of h-MoO_3 thin films using

seed layers and their photoluminescence properties [J]. Materials Science in Semiconductor Processing, 2022, 137: 106243.

[5] RAMAR V, KARTHIKEYAN B. Effect of reduced graphene oxide on the sunlight-driven photocatalytic activity of rGO/*h*-MoO_3 nanocomposites [J]. Journal of Physics D: Applied Physics, 2021, 54: 155502.

[6] SONG Yue-hong, ZHAO Yan, HUANG Zhi-fang, ZHAO Jing-zhe. Aqueous synthesis of molybdenum trioxide (*h*-MoO_3, *α*-$MoO_3·H_2O$ and *h*-/*α*-MoO_3 composites) and their photochromic properties study [J]. Journal of Alloys and Compounds, 2017, 693: 1290−1296.

[7] SHAFI P M, DHANABAL R, CHITHAMBARARAJ A, VELMATHI S, BOSE A C. *α*-MnO_2/*h*-MoO_3 hybrid material for high performance supercapacitor electrode and photocatalyst [J]. ACS Sustainable Chemistry & Engineering, 2017, 5: 4757−4770.

[8] PAVITRA V, SHIVANNA M, ALHARTHI F A, PRAVEEN B M, RAVIKIRAN Y T, BYRAPPA K, NAGARAJU G. High capacitive *h*-MoO_3 hexagonal rods and its applications towards lithium ion battery, humidity and nitrite sensing [J]. International Journal of Energy Research, 2021, 271: 115249−115259.

[9] SAKHUJA N, JHA R, BHAT N. Facile green synthesis of 2D hexagonal MoO_3 for selective detection of ammonia at room temperature [J]. Materials Science and Engineering B, 2021, 271: 115249.

[10] WANG Lu, ZHANG Guo-hua, SUN Yuan-jun, ZHOU Xin-wen, CHOU K C. Preparation of ultrafine *β*-MoO_3 from Industrial Grade MoO_3 Powder by the Method of Sublimation [J]. The Journal of Physical Chemistry C, 2016, 120: 19821−19829.

[11] KWAK D, WANG M, KOSKI K J, ZHANG L, SOKOL H, MARIC R, LEI Y. Molybdenum trioxide (*α*-MoO_3) nanoribbons for ultrasensitive ammonia (NH_3) gas detection: Integrated experimental and density functional theory simulation studies [J]. ACS Applied Materials & Interfaces, 2019, 11: 10697−10706.

[12] MO Y F, TAN Z G, SUN L P, LU Y B, LIU X Z. Ethanol-sensing properties of *α*-MoO_3 nanobelts synthesized by hydrothermal method [J]. Journal of Alloys and Compounds, 2020, 812: 152166.

[13] FARZI-KAHKESH S, RAHMANI M B, FATTAH A, Growth of novel *α*-MoO_3 hierarchical nanostructured thin films for ethanol sensing [J]. Materials Science in Semiconductor Processing, 2020, 120: 105263.

[14] WANG Lu, LI Meng-chao, QUE Biao-hua, XUE Zheng-liang, ZHANG Guo-hua. Oxidation roasting of molybdenite concentrate [J]. The Chinese Journal of Nonferrous Metals, 2021, 31: 1952−1964. (in Chinese)

[15] SUN Hu, LI Guang-hui, BU Qun-zhen, FU Zhong-qiao, LIU Hui-bo, ZHANG Xin, LUO Jun, RAO Ming-jun, JIANG Tao. Features and mechanisms of self-sintering of molybdenite during oxidative roasting [J]. Transactions of Nonferrous Metals Society of China, 2022, 32: 307−318.

[16] SILVEIRA J, MOURA J, LUZ-LIMA C,FREIRE P, SOUZA FILHO A. Laser-induced thermal effects in hexagonal MoO_3 nanorods [J]. Vibrational Spectroscopy, 2018, 98: 145−151.

[17] SONG Jin-mei, NI Xiao-min, GAO Li-sheng, ZHENG Hua-gui. Synthesis of metastable *h*-MoO_3 by simple chemical precipitation [J]. Materials Chemistry and Physics, 2007, 102: 245−248.

[18] KAMBLE B B, AJALKAR B D, TAWADE A K, SHARMAK K, MALI S S, HONG C. K, BATHULA C, KADAM A N, TAYADE S N. Ionic liquid assisted synthesis of *h*-MoO_3 hollow microrods and their application for electrochemical sensing of Imidacloprid pesticide in vegetables [J]. Journal of Molecular Liquids, 2021, 324: 115119.

[19] WU Zhuang-zhi, WANG De-zhi, LIANG Xun, SUN Ao-kui. Ultrasonic-assisted preparation of metastable hexagonal MoO_3 nanorods and their transformation to microbelts [J]. Ultrasonics Sonochemistry, 2011, 18: 288−292.

[20] BAI Shou-li, CHEN Song, CHEN Liang-yuan, ZHANG Ke-wei, LUO Rui-xian, LI Dian-qing, LIU C C. Ultrasonic synthesis of MoO_3 nanorods and their gas sensing properties [J]. Sensors and Actuators B: Chemical, 2012, 174: 51−58.

[21] ZHENG Lei, XU Yang, JIN Dong, XIE Yi. Novel metastable hexagonal MoO_3 nanobelts: Synthesis, photochromic, and electrochromic properties [J]. Chemistry of Materials, 2009, 21: 5681−5690.

[22] CHITHAMBARARAJ A, SANJINI N, VELMATHI S, BOSE A C. Preparation of *h*-MoO_3 and *α*-MoO_3 nanocrystals: Comparative study on photocatalytic degradation of methylene blue under visible light irradiation [J]. Physical Chemistry Chemical Physics, 2013, 15: 14761−14769.

[23] RAMANA C, ATUCHIN V, TROITSKAIA I, GROMILOV S, KOSTROVSKY V, SAUPE G. Low-temperature synthesis of morphology controlled metastable hexagonal molybdenum trioxide (MoO_3) [J]. Solid State Communications, 2009, 149: 6−9.

[24] DHAGE S, HASSAN M, YANG O B. Low temperature fabrication of hexagon shaped *h*-MoO_3 nanorods and its phase transformation [J]. Materials Chemistry and Physics, 2009, 114: 511−514.

[25] CHITHAMBARARAJ A, SANJINI N, BOSE A C, VELMATHI S. Flower-like hierarchical *h*-MoO_3: New findings of efficient visible light driven nano photocatalyst for methylene blue degradation [J]. Catalysis Science & Technology, 2013, 3: 1405−1414.

[26] ATUCHIN V, GAVRILOVA T, KOSTROVSKY V, POKROVSKY L, TROITSKAIA I. Morphology and structure of hexagonal MoO_3 nanorods [J]. Inorganic Materials, 2008, 44: 622−627.

[27] CHEN Xiao-hui, LEI Wei-wei, LIU Dan, HAO Jian, CUI Qi-liang, ZOU Guang-tian. Synthesis and characterization of hexagonal and truncated hexagonal shaped MoO_3 nanoplates [J]. The Journal of Physical Chemistry C, 2009, 113: 21582−21585.

[28] HUANG Xi-hu. Principles of iron and steel metallurgy [M]. Beijing: Metallurgical Industry Press, 2013. (in Chinese)

[29] QI Yan-yuan, CHEN Wen, MAI Li-qiang, HU Bin, DAI Ying. Growth mechanism of MoO_3 nanobelts under hydrothermal condition [J]. Chinese Journal of Inorganic Chemisty, 2007, 23: 1895−1900. (in Chinese)

[30] GAO Bin, FAN Hui-qing, ZHANG Xiao-jun, ZHU Chang-jun. Template-free hydrothermal synthesis of *α*-molybdenum trioxide nanobelts and their photocatalytic

activity for degradation of methylene blue [J]. Micro & Nano Letters, 2013, 8: 500−503.
[31] SONG Yue-hong, ZHAO Jing-zhe, ZHAO Yan, HUANG Zhi-fang, LI Ya-wen, WU Gong-juan. Synthesis of α-MoO_3 nanobelts with preferred orientation and good photochromic performance [J]. CrystEngComm, 2016, 18: 6502−6512.
[32] SONG Ji-mei, MEI Xue-feng, WANG hong, GAO Fei, ZHAO Shao-juan, HU Hai-qin. Synthesis via a HNO_3 assisted and photocatalytic property of hexagonal molybdenum trioxide [J]. China Molybdenum Industry, 2011, 35: 23−27. (in Chinese)
[33] JING Huan-ping, WANG Chong-chen, ZHANG Yi-wen, WANG Peng, LI Ran. Photocatalytic degradation of methylene blue in ZIF-8 [J]. RSC Advances, 2014, 4: 54454−54462.
[34] CHITHAMBARARAJ A, WINSTON B, SANJINI N, VELMATHI S, BOSE A C. Band gap tuning of h-MoO_3 nanocrystals for efficient visible light photocatalytic activity against methylene blue dye [J]. Journal of Nanoscience and Nanotechnology, 2015, 15: 4913−4919.
[35] LI Zhong-cheng, MA Jiao-jiao, ZHANG Bo, SONG Cai-xia, WANG De-bao. Crystal phase-and morphology-controlled synthesis of MoO_3 materials [J]. CrystEngComm, 2017, 19, 1479−1485.
[36] PHURUANGRAT A, THIPKONGLAS S, THONGTEM T, THONGTEM S. Hydrothermal synthesis and characterization of Dy-doped MoO_3 nanobelts for using as a visible-light-driven photocatalyst [J]. Materials Letters, 2017, 195: 37−40.
[37] JIN Yu-jian, LI Na, LIU Hai-qiu, HUA Xia, ZHANG Qiu-ying, CHEN Min-dong, TENG Fei. Highly efficient degradation of dye pollutants by Ce-doped MoO_3 catalyst at room temperature [J]. Dalton Transactions, 2014, 43: 12860−12870.
[38] SEN S K, PAUL T C, DUTTA S, HOSSAIN M, MIA M N H. XRD peak profile and optical properties analysis of Ag-doped h-MoO_3 nanorods synthesized via hydrothermal method [J]. Journal of Materials Science: Materials in Electronics, 2020, 31: 1768−1786.
[39] GUAN Xin, REN Yan-bing, CHEN Si-fan, YAN Jun-feng, WANG Gang, ZHAO Hong-yi, ZHAO Wu, ZHANG Zhi-yong, DENG Zhou-hu, ZHANG Yun-yao, DAI Yang, ZOU Lei-deng, CHEN Rui-yong, LIU Chun-li. Charge separation and strong adsorption-enhanced MoO_3 visible light photocatalytic performance [J]. Journal of Materials Science, 2020, 55: 5808−5822.

h-MoO_3 纳米棒和 h-/α-MoO_3 复合材料的制备及其光催化性能

王 璐[1]，李红肖[2]，薛正良[1,2]

1. 武汉科技大学 省部共建耐火材料与冶金国家重点实验室，武汉 430081；
2. 武汉科技大学 钢铁冶金及资源利用省部共建教育部重点实验室，武汉 430081

摘 要：提出一种合成 h-MoO_3 纳米棒和 h-/α-MoO_3 复合材料的简易湿法途径，并采用 XRD、TG−DSC、FESEM−EDX、TEM、FT-IR、拉曼、PL 和 UV−vis DRS 光谱等技术对所得产物进行表征。当所用原料液/固比为 2:1 和 5:1 时，能够合成单相 h-MoO_3 纳米棒；增加液/固比至 8:1 和 12:1，所得产物则为均质 h-/α-MoO_3 复合材料。根据实验结果，还对 h-MoO_3 的形成机理及其转换成 α-MoO_3 的反应过程进行研究。h-MoO_3 的淬火过程可分为 3 个不同的质量损失阶段，分别由物理吸附水、残留铵根离子以及结合水的移除所致。h-MoO_3 纳米棒和 h-/α-MoO_3 复合材料在亚甲基蓝染料的降解方面均显现出优异的可见光响应光催化性能。由于低的电子−空穴复合率、低的能带跃迁能以及强的吸附−光催化协同作用，h-/α-MoO_3 复合材料的光催化降解性能更为优异。

关键词：h-MoO_3；α-MoO_3；湿法合成；光催化性能；亚甲基蓝

(Edited by Bing YANG)